Available online at www.sciencedirect.com
SCIENCE DIRECT®
Journal of Computational Physics 216 (2006) 76–91
JOURNAL OF COMPUTATIONAL PHYSICS
www.elsevier.com/locate/jcp

Wall-driven incompressible viscous flow in a two-dimensional semi-circular cavity

R. Glowinski [a,b], G. Guidoboni [a,c,*], T.-W. Pan [a]

[a] Department of Mathematics, University of Houston, 651 Philip G. Hoffman Hall, Houston, TX 77204-3476, USA
[b] Laboratoire Jacques-Louis Lions, Université P. et M. Curie, 4 Place Jussieu, 75005, Paris, France
[c] Dipartimento di Matematica, Universitá di Ferrara, Via Machiavelli 35, 44100 Ferrara, Italy

Received 12 April 2005; received in revised form 15 November 2005; accepted 17 November 2005
Available online 4 January 2006

Dedicated to David Gottlieb on the occasion of his 60th anniversary.

Abstract

The main goal of this article is to investigate the capability of an operator-splitting/finite elements based methodology at handling accurately incompressible viscous flow at large Reynolds number (*Re*) in regions with corners and curved boundaries. To achieve this goal the authors have selected a wall-driven flow in a semi-circular cavity. On the basis of the numerical experiments reported in this article it seems that the method under investigation has no difficulty at capturing the formation of primary, secondary and tertiary vortices as *Re* increases; it has also the capability of identifying a Hopf bifurcation phenomenon taking place around $Re = 6600$.

1. Introduction

It is the opinion of these authors that, in the context of numerical methods for incompressible viscous flow, few problems have motivated such a large number of publications as the wall-driven square cavity one (actually, it has even motivated dedicated workshops where various solution methods have been compared). Reasons for this popularity are easy to identify, the main ones being that: (i) the flow region is two-dimensional and (ii) the simplicity of the geometry, and of the boundary conditions, gives an equal chance to various type of approximations and solution methods, such as finite differences, finite elements, spectral analysis, lattice Boltzmann, multi-grid, etc. The number of publications dedicated to the wall-driven incompressible viscous flow problem in a square cavity is so large that giving a comprehensive subset of the related references has become an impossible task; focusing on what we know best let us mention [1,2,6–8,14,16] (many of the various references therein are also worth consulting). Our primary goal here is to investigate the ability of the finite elements/operator-splitting techniques discussed in [8] at handling flow regions with corners and curved

* Corresponding author.
E-mail address: gio@math.uh.edu (G. Guidoboni).

0021-9991/$ - see front matter © 2005 Elsevier Inc. All rights reserved.
doi:10.1016/j.jcp.2005.11.021

boundaries, and this at Reynolds numbers large enough so that Hopf bifurcation phenomena may take place. To achieve the goal stated above, we selected a wall-driven semi-circular cavity flow problem thinking that, among other things, it will be interesting to see in what aspects the solutions of this new problem will differ from those of the previous one. A secondary goal is of course to introduce a new test problem, which we hope (without believing it very seriously) may become as popular as the other one. It is clear that the polar coordinate-based approximation method discussed in [3] applies to the problem considered here, however it relies on weighted Sobolev spaces more complicated to handle than the functional spaces employed in the present article; indeed, the numerical experiments presented in [3] correspond to Reynolds number much lower than those considered here.

The paper is organized as follows. In Section 2, we introduce the formulation of the problem and then we discuss the space and time discretizations in Section 3. Numerical results are presented in Section 4. They include a comparison with some experimental data presented in [13].

2. Formulation of the problem

An incompressible viscous fluid fills a semi-circular cavity where the straight part of the boundary Γ_1 is translating with an assigned velocity, the curvilinear part Γ_0 being motionless, see Fig. 1. The domain occupied by the fluid is then the two-dimensional region of space

$$\Omega = \left\{\mathbf{x} = (x_1, x_2) \in \mathbb{R}^2 \,|\, x_2 < 0,\ x_1^2 + x_2^2 < 1/4\right\}$$

and its flow in $\Omega \times (0, T)$, $T > 0$, is governed by the Navier–Stokes equations:

$$\nabla \cdot \mathbf{u} = 0, \tag{2.1}$$

$$\mathbf{u}_t + (\mathbf{u} \cdot \nabla)\mathbf{u} = -\nabla p + \nu \Delta \mathbf{u}, \tag{2.2}$$

equipped with the initial and boundary conditions:

$$\begin{aligned} &\mathbf{u}|_{t=0} = \mathbf{u}_0 \quad \text{with } \nabla \cdot \mathbf{u}_0 = 0 \text{ and } \mathbf{u}_0 \cdot \mathbf{n} = 0 \text{ on } \Gamma, \\ &\mathbf{u} = \mathbf{g} \text{ on } \Gamma \times (0, T) \quad \text{with } \int_\Gamma \mathbf{g}(t) \cdot \mathbf{n}\, d\Gamma = 0 \quad \text{on } (0, T). \end{aligned} \tag{2.3}$$

Here $\mathbf{u}$ and p are the flow velocity and pressure, ν is the fluid kinematic viscosity, while $\mathbf{n}$ is the unit outward normal vector at the boundary $\Gamma = \partial\Omega = \Gamma_1 \cup \Gamma_0$. In (2.3) (and below) we use the notation $\varphi(t)$ to denote the function $x \to \varphi(x, t)$.

We observe that since the upper wall is translating in the horizontal direction we have $\mathbf{g}(t) \cdot \mathbf{n} = 0$ on Γ_1 for $0 < t < T$, while $\mathbf{g}(t) = \mathbf{0}$ on Γ_0 for $0 < t < T$. Suppose now that in the neighborhood of the corners we regularize the wall velocity $\mathbf{g}$ by $\mathbf{g}_\delta$ (δ being a "small" parameter converging to zero) so that we have $\mathbf{g}_\delta(t) \cdot \mathbf{n} = 0\ \forall t$ and $\mathbf{g}_\delta(t) \in (H^{1/2}(\Gamma))^2$. In order to write a variational formulation for the problem (2.1)–(2.3) we first introduce the following functional spaces:

$$V_{\mathbf{g}(t)} = \{\mathbf{v} \,|\, \mathbf{v} \in (H^1(\Omega))^2,\ \mathbf{v} = \mathbf{g}(t) \text{ on } \Gamma\}, \tag{2.4}$$

$$V_0 = \{\mathbf{v} \,|\, \mathbf{v} \in (H^1(\Omega))^2,\ \mathbf{v} = \mathbf{0} \text{ on } \Gamma\}, \tag{2.5}$$

$$L^2_0(\Omega) = \{q \,|\, q \in L^2(\Omega),\ \int_\Omega q\, d\mathbf{x} = 0\}, \tag{2.6}$$

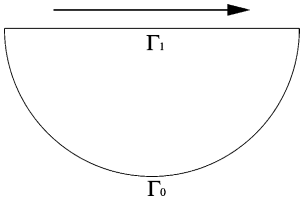

Fig. 1. Wall-driven flow in a semi-circular cavity.

after dropping the subscript δ from $\mathbf{g}_\delta$. The regularity of $\mathbf{g}$ implies that $V_{\mathbf{g}(t)}$ is not empty. Now, we multiply Eqs. (2.1) and (2.2) by the test functions $\mathbf{v} \in V_0$ and $q \in L^2(\Omega)$, respectively. The resulting equations are integrated over Ω to obtain the variational formulation of (2.1)–(2.3):

$$\begin{aligned}
&\text{For a.e. } t > 0, \text{ find } \mathbf{u}(t) \in V_{\mathbf{g}(t)}, p(t) \in L^2_0(\Omega), \text{ such that}\\
&\int_\Omega \mathbf{u}_t \cdot \mathbf{v}\,d\mathbf{x} + \int_\Omega (\mathbf{u}\cdot\nabla)\mathbf{u}\cdot\mathbf{v}\,d\mathbf{x} - \int_\Omega p\nabla\cdot\mathbf{v}\,d\mathbf{x} + \nu\int_\Omega \nabla\mathbf{u} : \nabla\mathbf{v}\,d\mathbf{x} = 0 \quad \forall \mathbf{v} \in V_0,\\
&\int_\Omega q\nabla\cdot\mathbf{u}\,d\mathbf{x} = 0 \quad \forall q \in L^2(\Omega),\\
&\mathbf{u}|_{t=0} = \mathbf{u}_0 \quad \text{with } \nabla\cdot\mathbf{u}_0 = 0.
\end{aligned} \tag{2.7}$$

If $\mathbf{g}(0)\cdot\mathbf{n} = \mathbf{u}_0\cdot\mathbf{n}$ (=0 here), one can show the existence of a solution for problem (2.7) (see for example the discussion in [10,11]).

3. Space and time discretizations

The domain Ω is clearly non-polygonal because of the curved portion Γ_0 of the boundary. To approximate velocity and pressure, we use here an isoparametric version (discussed in, e.g., [8, Chapter 5]) of the *Bercovier–Pironneau* finite elements method also known as the $P_1 - iso - P_2$ and P_1 finite elements approximation. This approximation was introduced in [4] and further discussed in, e.g., [9,15].

We introduce a triangulation $\mathscr{T}_h$ of the two-dimensional domain Ω with discretization step h and we decompose it as $\mathscr{T}_h = \mathscr{T}_{Rh} \cup \mathscr{T}_{0h}$, where

$$\mathscr{T}_{Rh} = \{T \,|\, T \in \mathscr{T}_h, \text{ the three edges of } T \text{ are rectilinear}\}, \tag{3.1}$$

$$\mathscr{T}_{0h} = \{T \,|\, T \in \mathscr{T}_h, \ T \text{ has one curvilinear edge with the two extremities on } \Gamma_0\}. \tag{3.2}$$

Every rectilinear triangle $T \in \mathscr{T}_{Rh}$ is divided into four sub-triangles K_{iT}, $i = 1,2,3,4$ by joining the midpoints of its edges. On the other hand, *every curved triangle* $T \in \mathscr{T}_{0h}$ is approximated by the quadrilateral $\widetilde{T}$ obtained by joining the midpoints of the two rectilinear edges and the midpoint of the curved one. Then, the quadrilateral $\widetilde{T}$ is divided into four sub-triangles K_{iT}, $i = 1,2,3,4$ as in the previous case (see Fig. 2).

To construct the velocity spaces we introduce

$$\widetilde{P}_2(T) = \begin{cases} \{q \,|\, q \in \mathscr{C}^0(T),\ q|_{K_{iT}} \in P_1,\ \forall i = 1,2,3,4\} & \text{if } T \in \mathscr{T}_{Rh},\\ \{q \,|\, q \in \mathscr{C}^0(\widetilde{T}), q|_{K_{iT}} \in P_1,\ \forall i = 1,2,3,4\} & \text{if } T \in \mathscr{T}_{0h}, \end{cases} \tag{3.3}$$

where $\mathscr{C}^0(T)$ (resp. $\mathscr{C}^0(\widetilde{T})$) is the space of the functions continuous over T (resp. $\widetilde{T}$), and P_1 is the space of polynomials with degree less or equal to one. Similarly, the following three-dimensional subspace of $\widetilde{P}_2(T)$ will be useful to construct the pressure spaces:

$$\widetilde{P}_1(T) = \{q \,|\, q \in \widetilde{P}_2(T),\ q(a_{ijT}) = (q(a_{iT}) + q(a_{jT}))/2,\ \forall i,j,\ 1 \leqslant i,j \leqslant 3,\ i \neq j\}, \tag{3.4}$$

where a_{iT}, $i = 1,2,3$, are the vertices of T, while a_{ijT}, with $i,j = 1,2,3$, are the midpoints of the (curved or rectilinear) edges of vertices a_{iT} and a_{jT}. We use the convention $a_{ijT} = a_{jiT}$, $\forall i,j$, $i \neq j$.

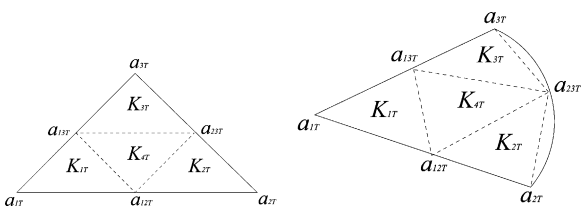

Fig. 2. Triangulation of the domain: subdivision of a rectilinear triangle (on the left) and of a curved triangle (on the right).

Thus, we define $\widetilde{\mathscr{T}}_{0h} = \{\widetilde{T}\}_{T\in\mathscr{T}_{0h}}$ and $\widetilde{\mathscr{T}}_h = \mathscr{T}_{Rh} \cup \widetilde{\mathscr{T}}_{0h}$; the discrete approximation of the domain Ω is given by $\Omega_h =$ interior of $\bigcup_{K\in\widetilde{\mathscr{T}}_h} K$ and $\Gamma_h = \partial\Omega_h$. Finally, we define the pressure and velocity finite element spaces as

$$P_h = \{q_h \,|\, q_h \in \mathscr{C}^0(\overline{\Omega}_h),\ q_h|_T \in P_1,\ \forall T \in \mathscr{T}_{Rh},\ q_h|_{\widetilde{T}} \in \widetilde{P}_1(T),\ \forall T \in \mathscr{T}_{0h}\}, \tag{3.5}$$

$$V_h = \{\mathbf{v}_h \,|\, \mathbf{v}_h \in (\mathscr{C}^0(\overline{\Omega}_h))^2,\ \mathbf{v}_h|_T \in (\widetilde{P}_2(T))^2,\ \forall T \in \mathscr{T}_{Rh},\ \mathbf{v}_h|_{\widetilde{T}} \in (\widetilde{P}_2(T))^2,\ \forall T \in \mathscr{T}_{0h}\}. \tag{3.6}$$

Let us now consider the time discretization. The main difficulties related to the numerical solution of problem (2.7) are: (a) the incompressibility condition and the related unknown pressure and (b) the advection term. Operator-splitting method allows to associate to each of them a specific operator and among the many

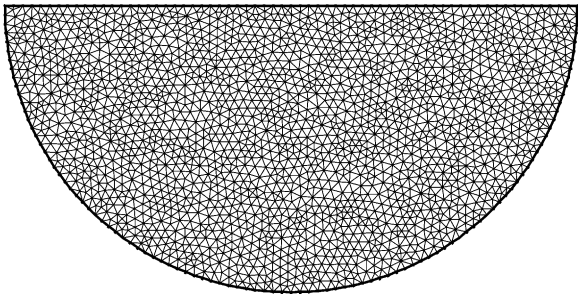

Fig. 3. Example of triangulation $\mathscr{T}_h$ on Ω.

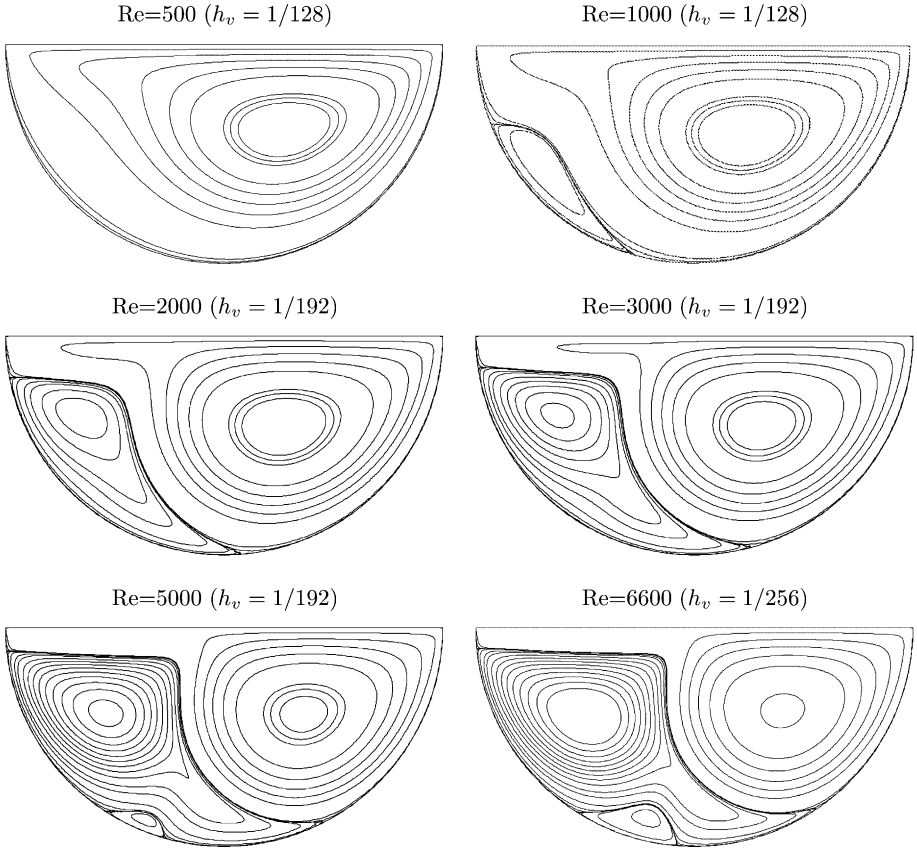

Fig. 4. Streamlines of the steady states reached for different Reynolds numbers.

versions available we advocate a very simple one which is first-order accurate [12]. The low-order accuracy is actually compensated by easy implementation, less cost in computational time, good stability and robustness properties.

Let Δt be the time discretization step and $t^n = n\Delta t$, $\mathbf{u}_h^n = \mathbf{u}_h(t^n)$, $p_h^n = p_h(t^n)$. Let us define the following spaces:

$$
\begin{aligned}
&V_{\mathbf{g}_h(t)} = \{\mathbf{v}_h \,|\, \mathbf{v}_h \in V_h,\ \mathbf{v}_h = \mathbf{g}_h(t) \text{ on } \Gamma_h\},\\
&V_{\mathbf{g}_h}^{n+1} = V_{\mathbf{g}_h(t^{n+1})},\\
&P_{0h} = \{q_h \,|\, q_h \in P_h,\ \int_{\Omega_h} q_h \,\mathrm{d}\mathbf{x} = 0\},\\
&V_{0h} = \{\mathbf{v}_h \,|\, \mathbf{v}_h \in V_h,\ \mathbf{v}_h = \mathbf{0} \text{ on } \Gamma_h\},\\
&V_{0h}^{n+1,-} = \{\mathbf{v}_h \,|\, \mathbf{v}_h \in V_h,\ \mathbf{v}_h = \mathbf{0} \text{ on } \Gamma_h^{n+1,-}\},\\
&\Gamma_h^{n+1,-} = \{\mathbf{x} \,|\, \mathbf{x} \in \Gamma_h,\ \mathbf{g}_h(t^{n+1}) \cdot \mathbf{n}(\mathbf{x}) < 0\}.
\end{aligned}
$$

For $n \geqslant 0$, $\mathbf{u}^n$ being known, the scheme consists of solving the following problems:

1. Find $\mathbf{u}^{n+1/3} \in V_{\mathbf{g}_h}^{n+1}$ and $p^{n+1/3} \in P_{0h}$ such that

$$
\begin{cases}
\int_{\Omega_h} \dfrac{\mathbf{u}^{n+1/3} - \mathbf{u}^n}{\Delta t} \cdot \mathbf{v}\,\mathrm{d}\mathbf{x} - \int_{\Omega_h} p^{n+1/3} \nabla \cdot \mathbf{v}\,\mathrm{d}\mathbf{x} = 0 \quad \forall \mathbf{v} \in V_{0h},\\
\int_{\Omega_h} q \nabla \cdot \mathbf{u}^{n+1/3}\,\mathrm{d}\mathbf{x} = 0 \quad \forall q \in P_h.
\end{cases}
\tag{3.7}
$$

2. Find $\mathbf{u}^{n+2/3} \in V_h$ via the solution of the following pure advection problem in $\Omega \times (t^n, t^{n+1})$

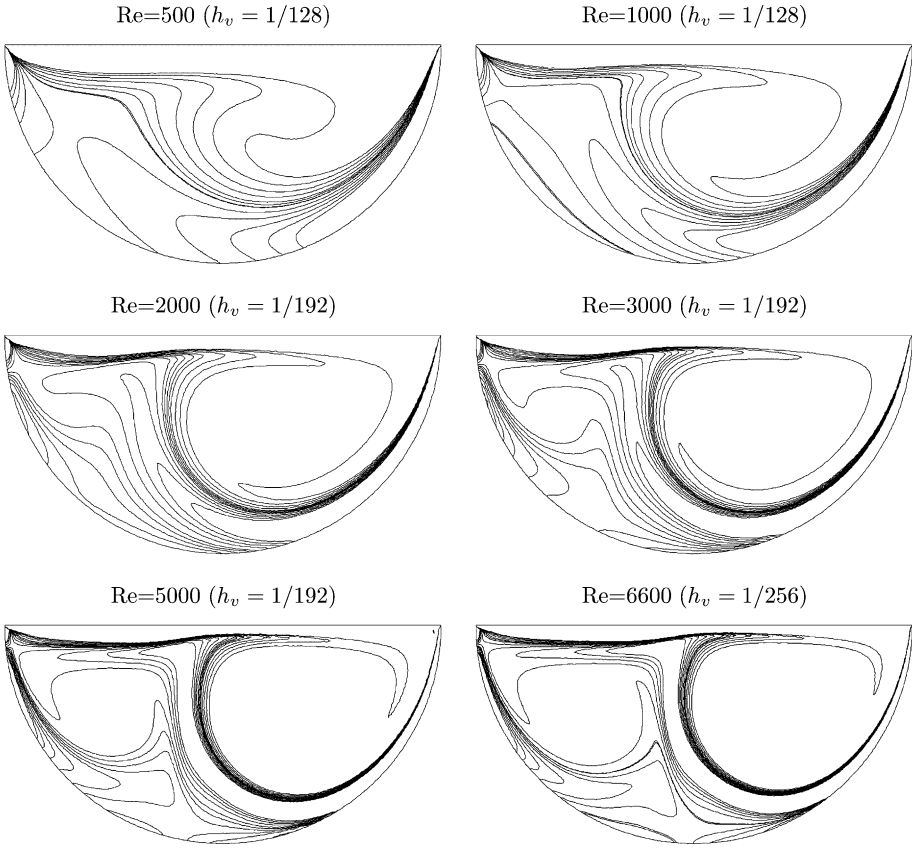

Fig. 5. Vorticity contours of the steady states reached for different Reynolds numbers.

$$\begin{cases} \int_{\Omega_h} \mathbf{u}_t \cdot \mathbf{v}\,d\mathbf{x} + \int_{\Omega_h} (\mathbf{u}^{n+1/3} \cdot \nabla)\mathbf{u} \cdot \mathbf{v}\,d\mathbf{x} = 0 \quad \forall \mathbf{v} \in V_{0h}^{n+1,-}, \\ \mathbf{u}(t^n) = \mathbf{u}^{n+1/3}, \\ \mathbf{u} = \mathbf{g}_h(t^{n+1}) \quad \text{on } \Gamma_h^{n+1,-} \times (t^n, t^{n+1}), \end{cases} \tag{3.8}$$

and then set $\mathbf{u}^{n+2/3} = \mathbf{u}(t^{n+1})$.

3. Find $\mathbf{u}^{n+1} \in V_{\mathbf{g}_h}^{n+1}$ such that

$$\int_{\Omega_h} \frac{\mathbf{u}^{n+1} - \mathbf{u}^{n+2/3}}{\Delta t} \cdot \mathbf{v}\,d\mathbf{x} + \nu \int_{\Omega_h} \nabla \mathbf{u}^{n+1} : \nabla \mathbf{v}\,d\mathbf{x} = 0 \quad \forall \mathbf{v} \in V_{0h}. \tag{3.9}$$

Above we have been assuming that $\mathbf{g}_h$ is an approximation of $\mathbf{g}$ continuous in space and time, vanishing at $(1/2, 0)$ and $(-1/2, 0)$, and such that $\mathbf{g}_h \cdot \mathbf{n} = 0$ on Γ_h.

The backward Euler's method has been used to derive the time discretization in (3.7) and (3.9). Problem (3.7) can be seen as a "*degenerated*" discrete Stokes problem (also called divergence free L^2-projection) for which efficient solution methods already exist as shown in, e.g., [8]. Problem (3.9) is a discrete elliptic system which is quite a classical problem. The advection step (3.8) has been solved using a wave-like equation method [5,8,14]: this approach (described in Appendix A) preserves the hyperbolic nature of advection, it does not introduce numerical dissipation and it is easy to implement. It consists in replacing problem (3.8) by the following wave-like equation one in $\Omega_h \times (t^n, t^{n+1})$:

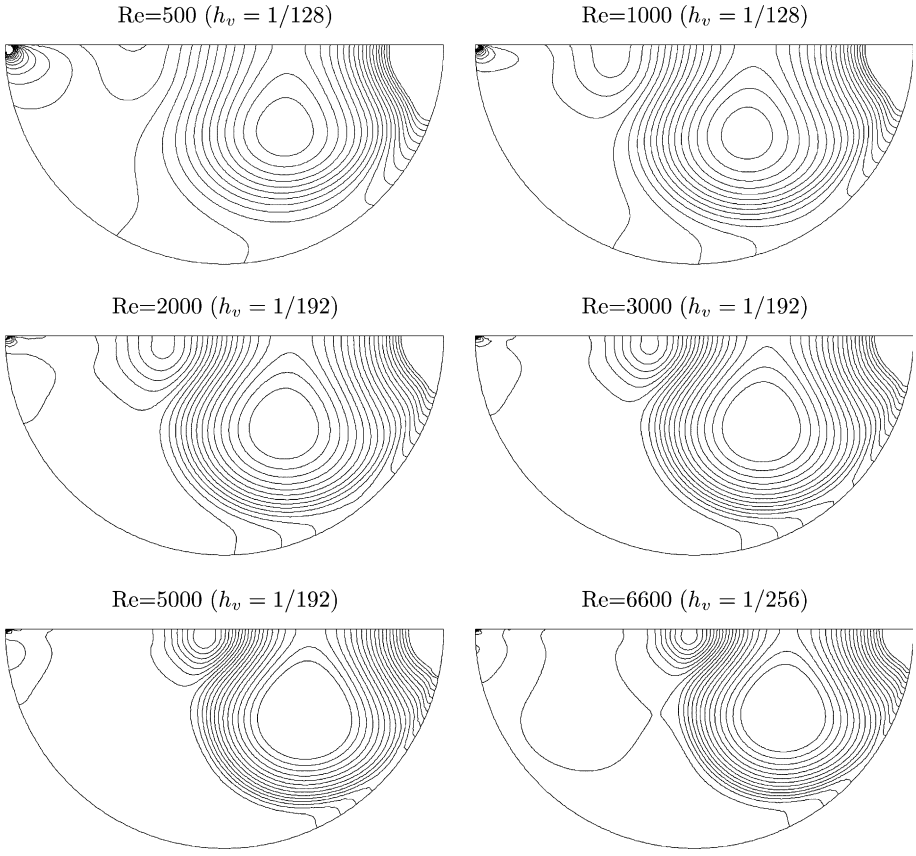

Fig. 6. Isobars of the steady states reached for different Reynolds numbers.

Table 1
Values used to plot the contours of the stream function, the vorticity and the pressure

Contours	Values
Stream function	-0.07, -0.0675, -0.065, -0.05, -0.04, -0.03, -0.02, -0.01, $\pm 1\times 10^{-4}$, $\pm 1\times 10^{-5}$, $\pm 1\times 10^{-7}$, -1×10^{-10}, 0.0, 1×10^{-8}, 1×10^{-6}, 5×10^{-4}, 0.001, 0.002, 0.003, 0.004, 0.005, 0.006, 0.007, 0.008, 0.009, 0.01
Vorticity	-4.85, -4.0, -3.0, -2.0, -1.0, -0.5, 0.0, 0.5, 1.0, 2.0, 3.0, 4.0, 5.0
Pressure	-0.1, -0.09, -0.08, -0.07, -0.06, -0.05, -0.04, -0.03, -0.02, -0.01, 0.0, 0.01, 0.02, 0.03, 0.04, 0.05, 0.06, 0.07, 0.08, 0.09, 0.1

$$\begin{cases} \int_{\Omega_h} \mathbf{u}_{tt}\cdot\mathbf{v}\,d\mathbf{x} + \int_{\Omega_h}(\mathbf{u}^{n+1/3}\cdot\nabla)\mathbf{u}\cdot(\mathbf{u}^{n+1/3}\cdot\nabla)\mathbf{v}\,d\mathbf{x} + \int_{\Gamma_h\setminus\Gamma_h^{n+1,-}}(\mathbf{g}_h(t^{n+1})\cdot\mathbf{n})(\frac{\partial\mathbf{u}}{\partial t}\cdot\mathbf{v})\,d\Gamma = 0 \quad \forall\mathbf{v}\in V_{0h}^{n+1,-},\\ \mathbf{u}(t^n) = \mathbf{u}^{n+1/3},\\ \int_{\Omega_h}\mathbf{u}_t(t^n)\cdot\mathbf{v}\,d\mathbf{x} = -\int_{\Omega_h}(\mathbf{u}^{n+1/3}\cdot\nabla)\mathbf{u}^{n+1/3}\cdot\mathbf{v}\,d\mathbf{x} \quad \forall\mathbf{v}\in V_{0h}^{n+1,-},\ \ \mathbf{u}_t(t^n)\in V_{0h}^{n+1,-},\\ \mathbf{u} = \mathbf{g}_h(t^{n+1}) \quad \text{on } \Gamma_h^{n+1,-}\times(t^n,t^{n+1}). \end{cases} \tag{3.10}$$

We have solved problem (3.10) using a second-order accurate time discretization scheme which is discussed in, e.g., [8, Chapter 6] and [14]. For those readers wondering why to use a second-order accurate scheme while the global scheme is first order, let us say that: (1) the second order centered in space-centered in time scheme that we use is the simplest one we can think of. It is explicit if one uses numerical integration to have a diagonal mass matrix with the term $\mathbf{u}_{tt}$; (2) being non-dissipative, the above scheme does not introduce numerical viscosity as upwinding schemes do, and even as the method of characteristic does (albeit much less).

Table 2
Location of the point where the minimum $\psi_{\min}$ of the stream function is reached at different Re with mesh size h_v

Re	h_v	$\psi_{\min}$	Location
1000	1/128	-0.0780	$(0.6156,-0.2029)$
2000	1/192	-0.0765	$(0.6329,-0.2042)$
3000	1/192	-0.0747	$(0.6548,-0.2031)$
5000	1/192	-0.0726	$(0.6809,-0.1988)$
6600	1/256	-0.0673	$(0.7006,-0.1894)$

Table 3
Location of the point where the minimum $\psi_{\min}$ of the stream function is reached at different Re with smaller mesh size h_v

Re	h_v	$\psi_{\min}$	Location
1000	1/192	-0.0779	$(0.6214,-0.2030)$
2000	1/256	-0.0763	$(0.6359,-0.2052)$
3000	1/256	-0.0742	$(0.6514,-0.2027)$
5000	1/256	-0.0700	$(0.6833,-0.1936)$
6600	1/300	-0.0670	$(0.7009,-0.1891)$

Table 4
Angles of detachment of the secondary vortex (the angles are given in degrees)

Re	θ_1	θ_2
1000	21.42	71.49
1500	14.21	86.51
2000	10.78	94.34
2500	9.54	100.30
3000	7.77	104.53

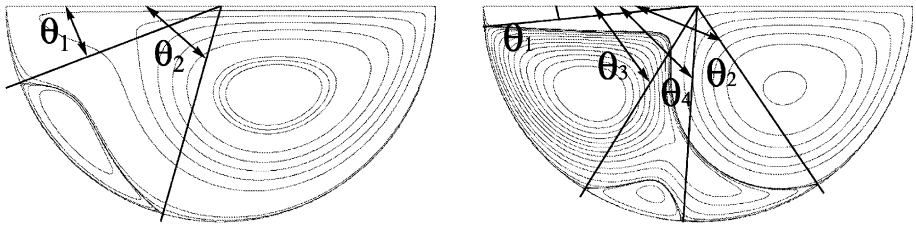

Fig. 7. Sketches of the angular variables for the locations of the separation and reattachment points.

4. Numerical experiments

The investigation of the stability of this wall-driven cavity flow is performed by running simulations for different values of the Reynolds number Re defined as $Re = UD/v$, where U is the characteristic velocity of the fluid, D is the characteristic length of the domain and v is the kinematic viscosity of the fluid. We have taken U equal to the norm of the sliding velocity of the upper wall and D equal to the diameter of the cavity,

Table 5
Angles of detachment of the secondary and tertiary vortices (the angles are given in degrees)

Re	θ_1	θ_3	θ_4	θ_2
5000	6.70	57.54	73.84	117.09
5500	6.70	57.54	78.67	118.96
6000	5.59	58.15	81.48	122.42
6500	5.59	58.15	85.13	123.41

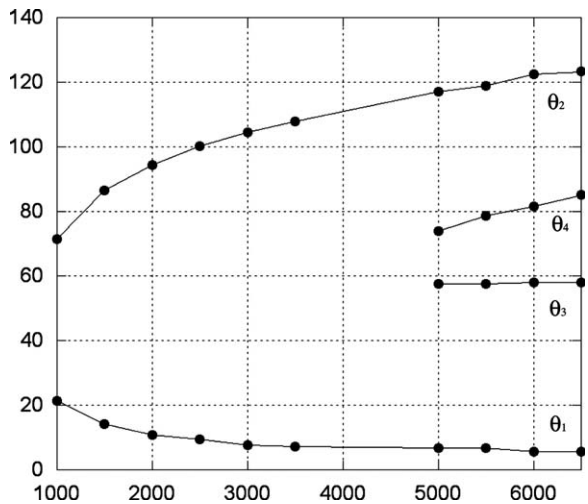

Fig. 8. Variation of the angles of detachment of the vortices as a function of the Reynolds number (the angles are given in degrees).

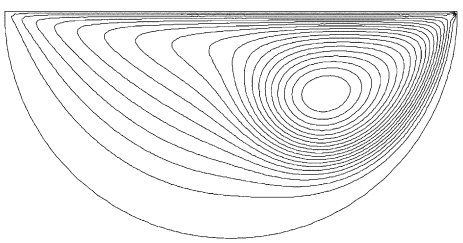

Fig. 9. Streamlines computed for $Re = 1000$ at $t = 3.48$.

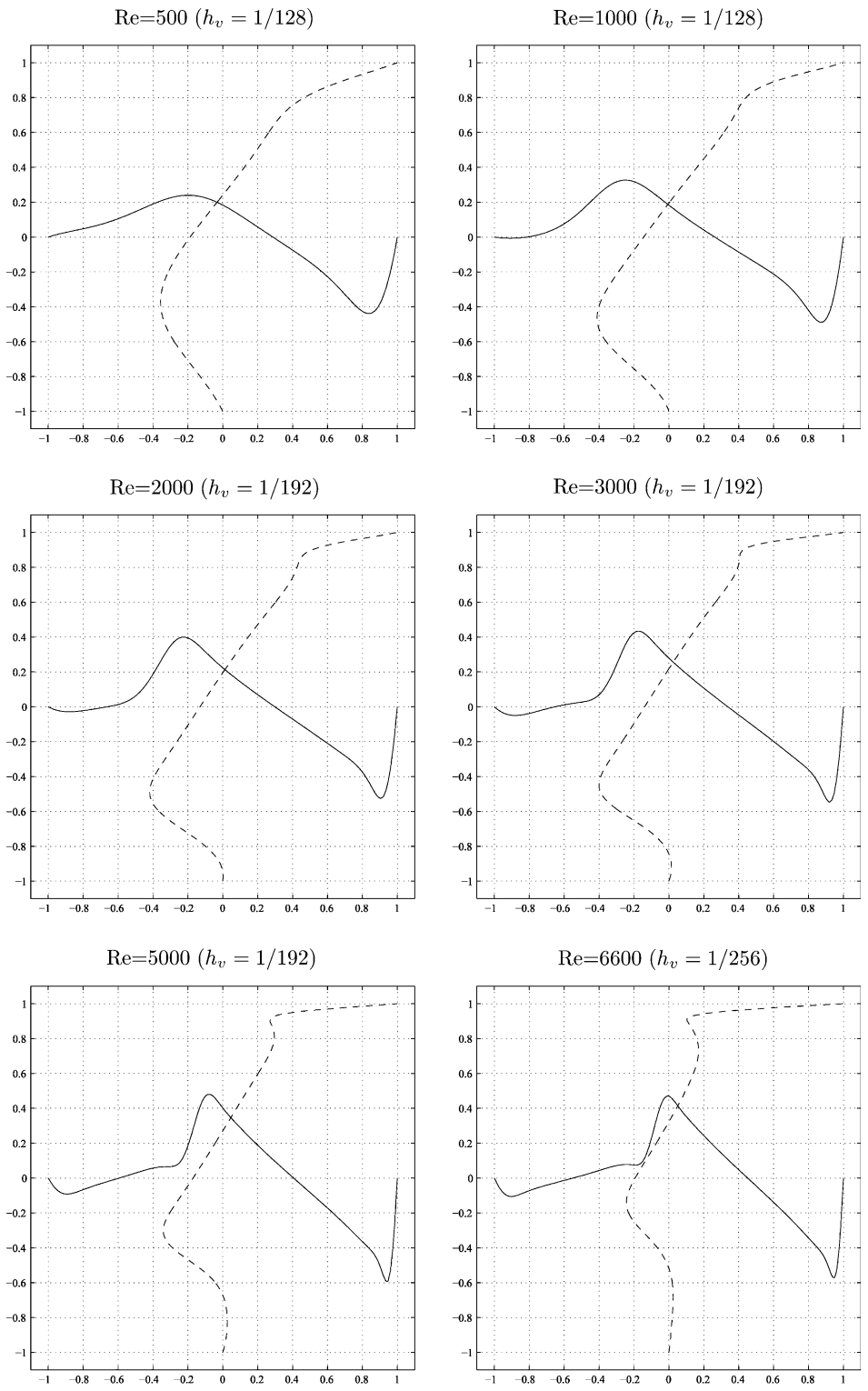

Fig. 10. The dashed line represents the u_1-velocity component along the line $x_1 = 1/2$, while the solid line represents the u_2-velocity component along the line $x_2 = -1/4$.

implying therefore that $U = 1$ and $D = 1$. Finally, in the particular case considered here, the Reynolds number reduces to $Re = 1/\nu$.

We take the Dirichlet data for the velocity in the form:

$$\mathbf{g}(t) = \begin{cases} \phi(t)\mathbf{e}_1 & \text{on } \Gamma_1, \\ \mathbf{0} & \text{on } \Gamma_0, \end{cases} \tag{4.1}$$

where $\mathbf{e}_1 = (1,0)$ and

$$\phi(t) = \begin{cases} 1 - \mathrm{e}^{-20t} & \text{if } 0 < t \leqslant 0.5, \\ 1, & \text{if } t > 0.5. \end{cases} \tag{4.2}$$

It follows from (4.1) that $\Gamma^{n+1,-} = \emptyset$, implying in turn that $V_{0h}^{n+1,-} = V_h$. The above data have been smoothed in time to avoid possible difficulties associated with a genuine impulse. Concerning the initial conditions, we take $\mathbf{u}_0 = \mathbf{0}$ for $Re = 500$ and then for other values of Re we take as $\mathbf{u}_0$ the steady-state solution obtained at the previous Reynolds number in the sequence 500, 1000, 2000, 3000, 5000 and 6000. When the Reynolds number is large enough, the solution does not reach a steady state any more but shows an oscillatory behavior: we then proceed by bisection to narrow the range of Re for which the Hopf bifurcation occurs.

For the time discretization, we have taken $\Delta t = 0.0005$. As mentioned in Section 3, we solve the advection step using a wave-like equation method which requires the specification of a time substep: here we have chosen it equal to $\Delta t/5$. The velocity $\mathbf{u}$ has been approximated by continuous piecewise affine vector-valued functions on a triangulation $\mathscr{T}_h$, like the one shown in Fig. 3, with mesh size h_v. The pressure is defined on a triangulation twice coarser. In the simulations, the solution is considered a steady state when the following condition is satisfied:

$$\frac{\|\mathbf{u}^n - \mathbf{u}^{n-1}\|_{L^2(\Omega)}}{\|\mathbf{u}^n\|_{L^2(\Omega)}} < 10^{-7}. \tag{4.3}$$

Table 6
Selected numerical values of the u_1-velocity component along the line $x_1 = 1/2$

x_2	$Re = 500$	$Re = 1000$	$Re = 2000$	$Re = 3000$	$Re = 5000$	$Re = 6600$
0.00000	1.00000	1.00000	1.00000	1.00000	1.00000	1.00000
−0.05010	0.46625	0.44242	0.42521	0.39517	0.29522	0.15920
−0.10020	0.26222	0.31359	0.30099	0.26678	0.20265	0.14022
−0.15030	0.12258	0.16051	0.14456	0.12047	0.07784	0.04243
−0.20040	−0.03376	0.00301	0.00185	−0.01272	−0.04437	−0.07306
−0.25050	−0.18879	−0.14617	−0.13209	−0.14042	−0.17134	−0.19506
−0.30060	−0.31375	−0.29153	−0.26443	−0.26917	−0.30537	−0.23003
−0.35070	−0.35530	−0.40361	−0.39444	−0.39163	−0.28595	−0.06390
−0.40080	−0.27589	−0.35822	−0.36203	−0.27661	−0.04091	0.01971
−0.50000	0.00000	0.00000	0.00000	0.00000	0.00000	0.00000

Table 7
Selected numerical values of the u_2-velocity component along the line $x_2 = -1/4$

x_1	$Re = 500$	$Re = 1000$	$Re = 2000$	$Re = 3000$	$Re = 5000$	$Re = 6600$
0.06699	0.00000	0.00000	0.00000	0.00000	0.00000	0.00000
0.23880	0.10367	0.07459	0.01216	0.01037	−0.00305	−0.01452
0.32558	0.18824	0.24697	0.18202	0.06717	0.05610	0.04230
0.41236	0.23944	0.31890	0.39541	0.42304	0.17885	0.07508
0.49913	0.18411	0.18388	0.22515	0.28061	0.40440	0.46982
0.58591	0.05868	0.04097	0.07049	0.10814	0.18982	0.24504
0.67268	−0.07432	−0.08632	−0.06988	−0.04622	0.00598	0.04843
0.75946	−0.22684	−0.21315	−0.20941	−0.19815	−0.17138	−0.13862
0.84624	−0.42578	−0.42124	−0.37485	−0.36123	−0.36417	−0.34359
0.93301	0.00000	0.00000	0.00000	0.00000	0.00000	0.00000

Steady states were reached for Reynolds numbers up to 6600. Streamlines, vorticity contours and isobars of the steady states reached for $Re = 500$, 1000, 2000, 3000, 5000 and 6600 are reported in Figs. 4–6 together with the mesh size used. The values used to plot the contours are listed in Table 1. When the Reynolds number is small, the final steady state consists of one vortex only (see $Re = 500$ in Fig. 4). As the Reynolds number increases, first a secondary vortex and then a tertiary vortex arise, as we can see in Fig. 4. The size of the vortices depends on the Reynolds number too.

In the square cavity, a major vortex is occupying the central part of the domain, while minor vortices appear at the lower corners and at the top-left (see e.g. [14]). In the case of semi-circular cavity, the vortices are developing at the bottom and as the Reynolds number increases, they grow pushing the main vortex to the right part of the cavity. Actually this phenomenon is tracked by the point where the minimum value of the stream function Ψ is attained. In Table 2, we have summarized the minimum value of Ψ and its location for the steady states reached at $Re = 1000$, 2000, 3000, 5000 and 6600, computed with mesh size $h_v = 1/128$, 1/192, 1/192, 1/192, 1/256, respectively.

We repeated the computations using finer meshes and the results agree with those previously obtained in terms of streamlines, vorticity contours and isobars of the steady states reached at different Reynolds numbers.

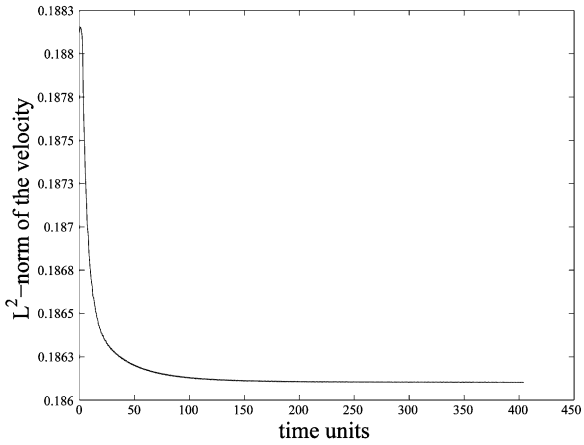

Fig. 11. Evolution of the L^2-norm of the velocity before the Hopf bifurcation ($Re = 6600$).

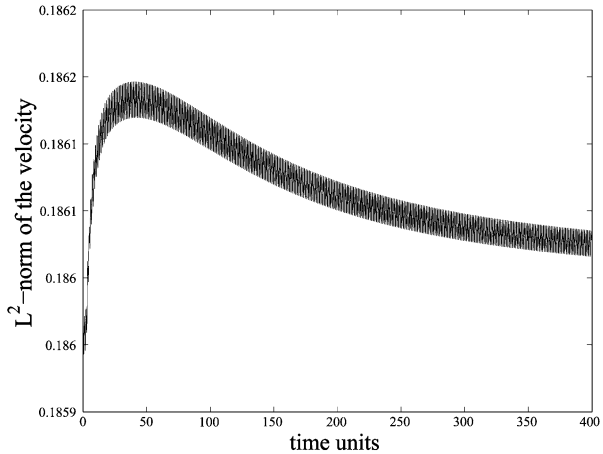

Fig. 12. Evolution of the L^2-norm of the velocity beyond the Hopf bifurcation ($Re = 6650$).

In Table 3, we have reported the minimum value of the stream function and its location computed at different Reynolds number using the set of finer meshes.

It took about 3.84 s/time step to run the simulations at $Re = 5000$, $h_v = 1/256$ with 31,952 vertices and 63,244 triangles for the velocity mesh, on a AMD Opteron(tm) Processor 248, CPU 2.2 GHz.

The location of the secondary and tertiary vortices is identified by the position of their end points on the curved edge of the cavity. In Table 4, we have collected the results for Reynolds numbers between 1000 and 3000: in this range the solution evolves to a steady state with a secondary vortex only. Then the angles θ_1 and θ_2 reported in the table are the angles with respect to the center of the disk between the upper-left corner and the points on the curved boundary where the secondary vortex starts and ends, respectively, as shown in Fig. 7. When the Reynolds number exceeds 5000 then a tertiary vortex appears and the results are shown in Table 5. Here θ_1 and θ_2 are the angles locating the secondary vortex, while θ_3 and θ_4 correspond to the tertiary vortex, see Fig. 7. A recapitulative graph is drawn in Fig. 8.

Experiments performed by Migeon et al. [13] show that the shape of the flow establishment phase in a lid-driven semi-circular cavity at $Re = 1000$ consists of only one recirculation vortex, without any secondary flow

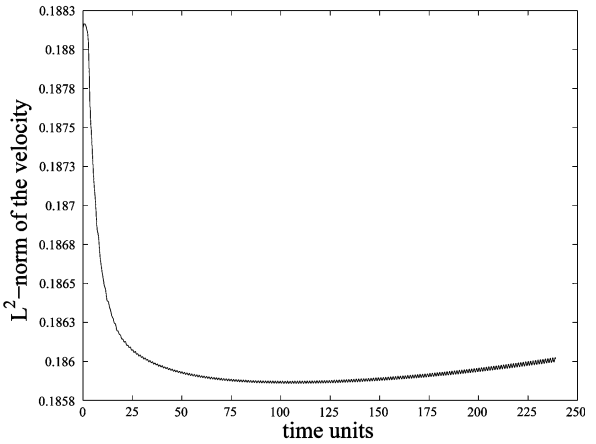

Fig. 13. Evolution of the L^2-norm of the velocity beyond the Hopf bifurcation ($Re = 6700$).

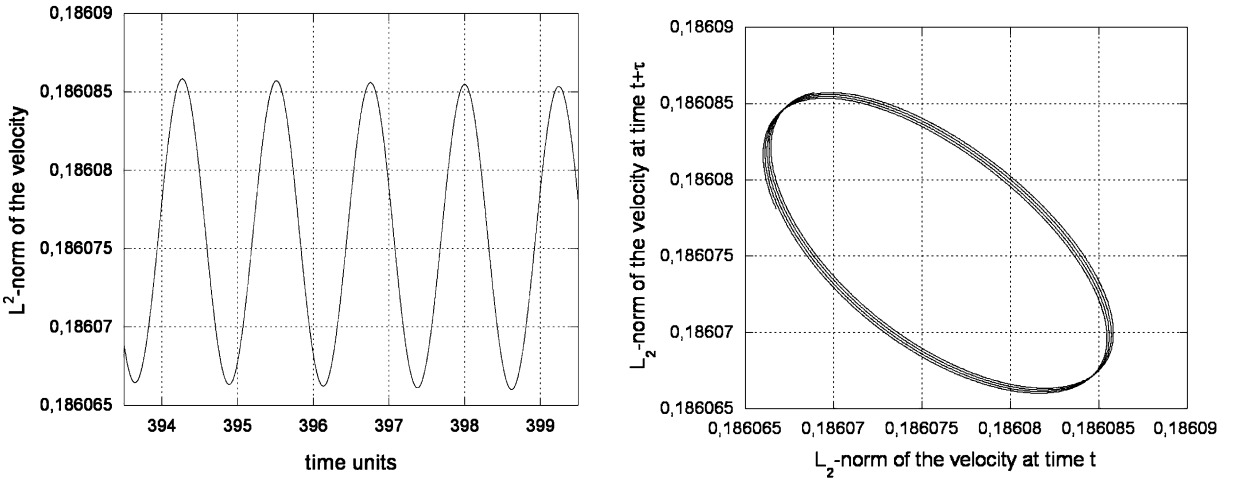

Fig. 14. Oscillations in time of the L^2-norm of the velocity for $Re = 6650$ (on the left). Two-dimensional phase portrait of the L^2-norm of the velocity at $Re = 6650$, $\tau = 0.8$ (on the right).

recirculation zone. Their final time of observation is $t^* = 12$, where $t^* = V_0 t/B$ is a dimensionless time, t being the physical time, $V_0 = 1.8$ cm/s the constant speed of the sliding cavity wall and $B = 6.2$ cm the diameter of the cavity. Therefore, the final physical time of observation is $t = 3.48$. In Fig. 9, we report the streamlines computed with our numerical scheme for $Re = 1000$ at $t = 3.48$ and their agreement is very satisfactory, at least qualitatively (see [13, Fig. 5, p. 476]). Our numerical computations show that a secondary vortex will eventually appear, actually its formation begins approximately at $t \simeq 6$.

In Fig. 10, we have plotted in dashed line the u_1-velocity component along the line $x_1 = 1/2$ (the values are meant to be read on the horizontal axis), while the solid line represents the u_2-velocity component along the line $x_2 = -1/4$ (the values are meant to be read on the vertical axis). As shown in Fig. 3, our mesh is not structured and therefore the curves in Fig. 10 have been obtained via interpolation. A selection of the interpolated numerical values corresponding to the profiles in Fig. 10 are listed in Tables 6 and 7.

At $Re = 6650$, we are beyond a Hopf bifurcation point. We have reported in Figs. 11–13 the evolution of the L^2-norm of the velocity in the neighborhood of the critical point. For $Re = 6600$, a steady state is reached: the L^2-norm of the velocity gets flat and eventually condition (4.3) is verified around $t = 400$. As Re exceeds 6650, the L^2-norm of the velocity shows an oscillatory behavior. In Fig. 14, we draw a more detailed picture of these oscillations for $Re = 6650$. We also show a phase portrait obtained by plotting the L^2-norm of the velocity at time t and at a delayed time $t + \tau$, as in [2]. The choice $\tau = 0.8$ leads to the graph in Fig. 14. In order to

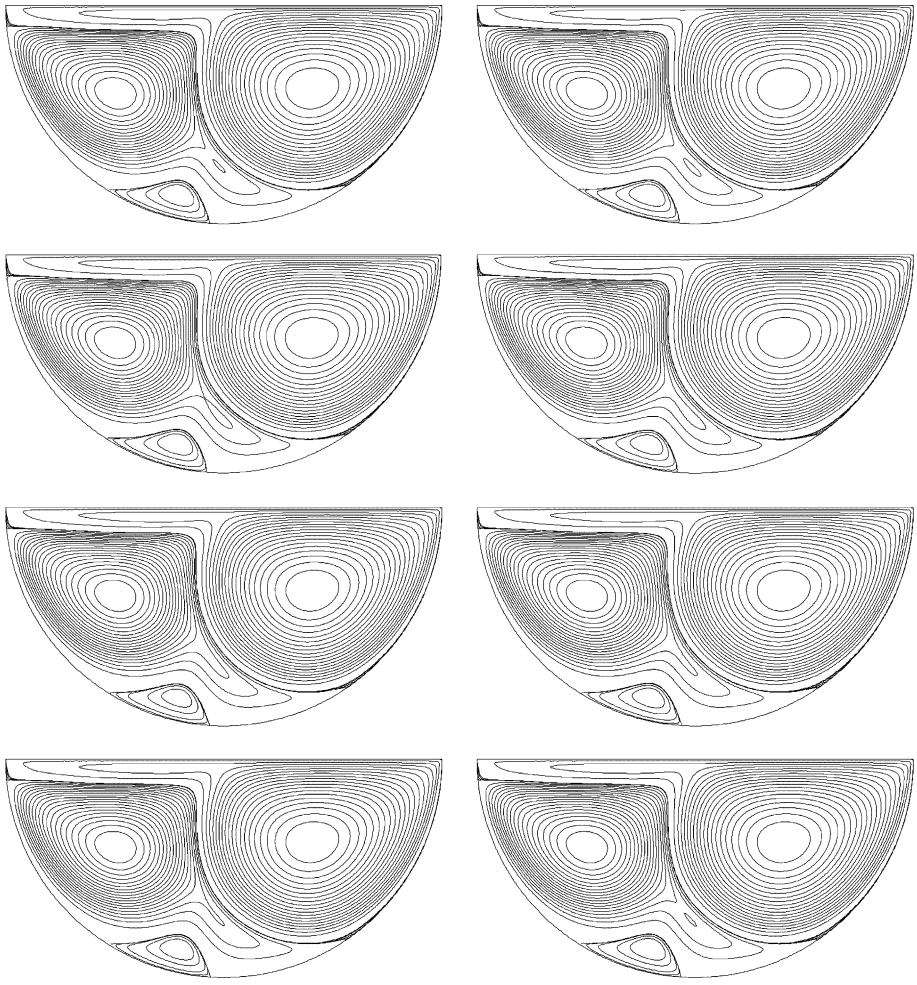

Fig. 15. One complete cycle of streamlines contours (from left to right, from top to bottom; $Re = 6700$).

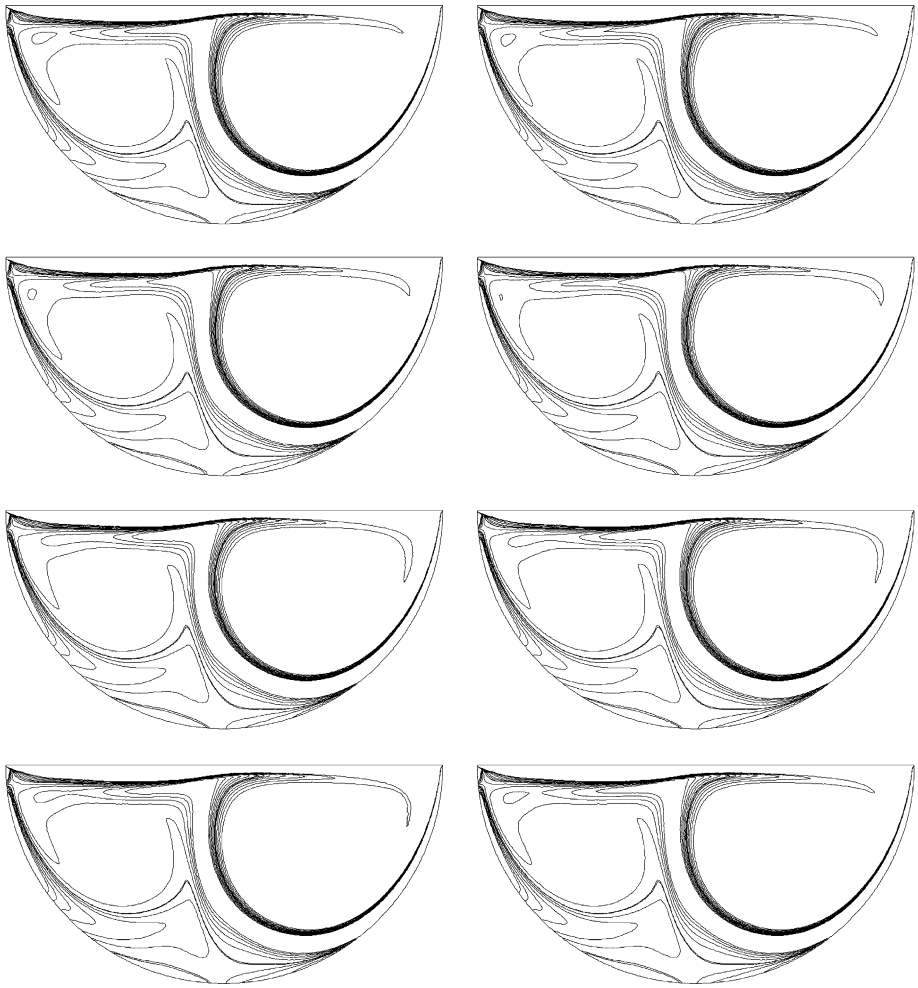

Fig. 16. One complete cycle of vorticity contours (from left to right, from top to bottom; $Re = 6700$).

ensure that the computed periodic solution is not a numerical artifact, we have performed simulations at $Re = 6650$ with three sets of mesh size and time step, namely $(h_v, \Delta t) = (1/256, 5 \times 10^{-4})$, $(h_v, \Delta t) = (1/300, 5 \times 10^{-4})$, $(h_v, \Delta t) = (1/256, 2.5 \times 10^{-4})$. For the substep in the advective part, we have always kept $\Delta t/5$. As period of the oscillations for the different settings, we found 1.243, 1.241 and 1.229, respectively. In addition, the period appears to be a non-decreasing function of the Reynolds number: for $Re = 6700$, 7000, 8000 the period is 1.243, 1.244, 1.262, respectively.

In Fig. 15, we have plotted eight pictures of the streamlines contours showing the evolution of the solution at $Re = 6700$ during one whole period. The most significant change is the oscillation of the secondary and tertiary vortices in the lower part of the cavity. The evolution of the vorticity contours is shown in Fig. 16. Here oscillations appears at the upper corners. The behavior of isobars during one period offers the most pronounced oscillatory pattern. In Fig. 17, we can see that the isobar located in the left half of the cavity is splitting and merging with the isobar at its right.

Acknowledgments

The first and the third authors were supported by NSF (Grant DMS-0209066), while the second author was supported by the Fulbright Research Scholarship 15032421. The authors thank also the reviewers of this article for their most helpful comments and suggestions.

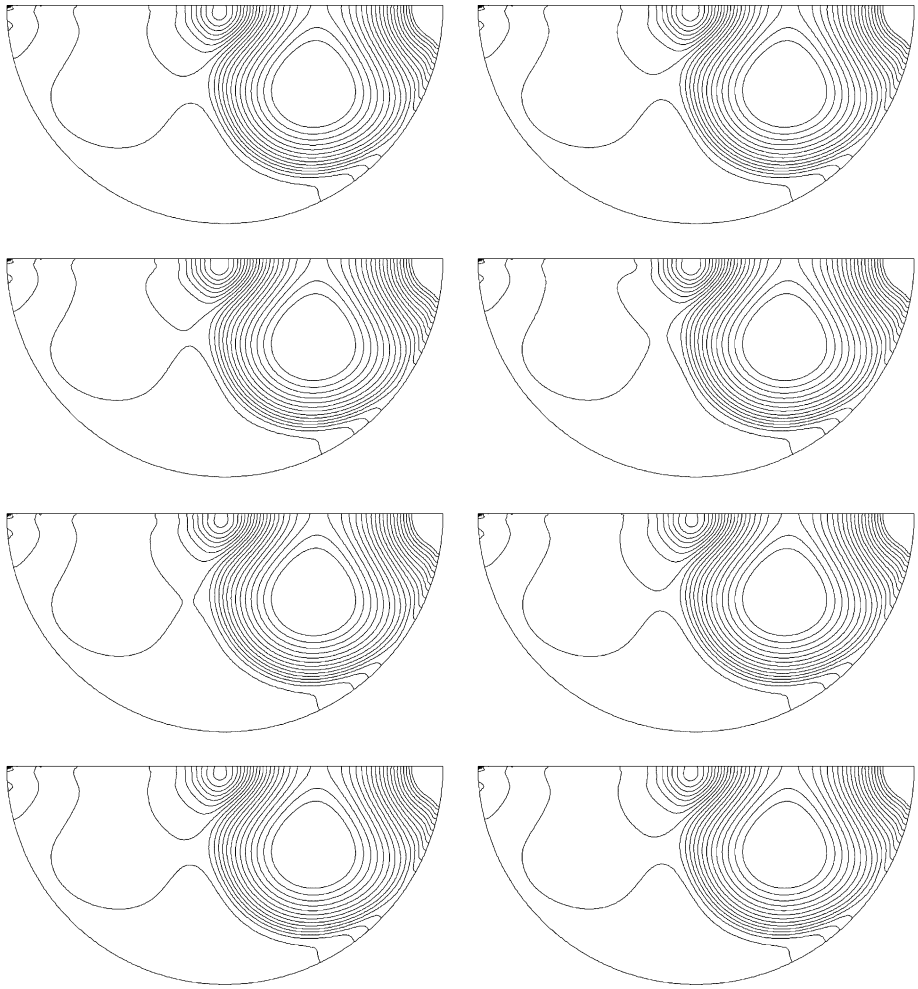

Fig. 17. One complete cycle of isobars (from left to right, from top to bottom; $Re = 6700$).

Appendix A

In Section 3, we mentioned that we used a so-called "wave-like equation" method to solve the advection subproblems (3.8) obtaining thus the subproblems (3.10). Owing to the importance of the wave-like equation concerning this article, we are going to discuss it in this Appendix A.

Problem (3.8) follows from the space discretization of

$$\begin{cases} \mathbf{u}_t + (\mathbf{u}^{n+1/3} \cdot \nabla)\mathbf{u} = \mathbf{0} \quad \text{in } \Omega \times (t^n, t^{n+1}), \\ \mathbf{u} = \mathbf{g}(t^{n+1}) \quad \text{on } \Gamma^{n+1,-} \times (t^n, t^{n+1}), \\ \mathbf{u}(t^n) = \mathbf{u}^{n+1/3} \end{cases} \tag{A.1}$$

with $\Gamma^{n+1,-} = \{\mathbf{x} | \mathbf{x} \in \Gamma, \mathbf{g}(t^{n+1}) \cdot \mathbf{n} < 0\}$, and $\nabla \cdot \mathbf{u}^{n+1/3} = 0$. For the particular problem discussed in this article, the set $\Gamma^{n+1,-}$ is empty, however, for the sake of generality, we keep here the possibility of $\Gamma^{n+1,-} \neq \emptyset$.

The components of the solution $\mathbf{u}$ of problem (A.1) are solutions of a pure advection problem of the following form:

$$\begin{cases} \varphi_t + \mathbf{V} \cdot \nabla\varphi = 0 \quad \text{in } \Omega \times (t^n, t^{n+1}), \\ \varphi = g \quad \text{on } \Gamma^- \times (t^n, t^{n+1}), \\ \varphi(t^n) = \varphi_0 \end{cases} \tag{A.2}$$

where (i) The functions g and φ_0 are given, with $g_t = 0$. (ii) $\nabla \cdot \mathbf{V} = 0$ with $\mathbf{V}_t = 0$. (iii) The subset Γ^- of $\partial\Omega$ is defined by $\Gamma^- = \{\mathbf{x} \,|\, \mathbf{x} \in \Gamma, \mathbf{V}(\mathbf{x}) \cdot \mathbf{n}(\mathbf{x}) < 0\}$, $\mathbf{n}$ being the outward unit normal vector at Γ.

We can easily show that (A.2) implies (formally, at least) that for a.e. $t \in (t^n, t^{n+1})$ we have

$$\int_\Omega \varphi_{tt} v \, d\mathbf{x} + \int_\Omega (\mathbf{V} \cdot \nabla\varphi)(\mathbf{V} \cdot \nabla v) \, d\mathbf{x} + \int_{\Gamma \setminus \Gamma^-} \mathbf{V} \cdot \mathbf{n} \, \varphi_t v \, d\Gamma = 0 \quad \forall v \in H^{1,-}(\Omega), \tag{A.3}$$

where $H^{1,-}(\Omega) = \{v \,|\, v \in H^1(\Omega), v = 0 \text{ on } \Gamma^-\}$, with the boundary and initial conditions:

$$\varphi = g \quad \text{on } \Gamma^- \times (t^n, t^{n+1}), \tag{A.4}$$

$$\varphi(t^n) = \varphi_0, \quad \varphi_t(t^n) = -\mathbf{V} \cdot \nabla\varphi_0. \tag{A.5}$$

Actually, relation (A.3) implies that

$$\mathbf{V} \cdot \mathbf{n}(\varphi_t + \mathbf{V} \cdot \nabla\varphi) = 0 \quad \text{on } (\Gamma \setminus \Gamma^-) \times (t^n, t^{n+1}), \tag{A.6}$$

which is, clearly, a kind of generalized Neumann boundary condition (perfectly absorbing for the pure advection problem considered here). As shown in, e.g., [6] or [8, Chapter 6], the formulation (A.3)–(A.5) of problem (A.2) is well-suited to solution methods via standard finite element approximations like the globally continuous and piecewise affine ones used to compute the velocity in (3.7) and (3.9).

References

[1] J.H. Argyris, P.C. Dunne, The finite element method applied to fluid mechanics, in: B.L. Hewitt, C.R. Illingworth, R.C. Lock, K.W. Mangler, J.M. Mc Donnel, C. Richards, J. Walkden (Eds.), Computational Methods and Problems in Aeronautical Fluid Dynamics, Academic Press, London, 1976, pp. 158–197.

[2] F. Auteri, N. Parolini, L. Quartapelle, Numerical investigation on the stability of the singularly driven cavity flow, J. Comput. Phys. 183 (1) (2002) 1–25.

[3] Z. Belhachmi, C. Bernardi, A. Karageorghis, Spectral element discretization of the circular driven cavity. Part IV: The Navier–Stokes equations, J. Math. Fluid Mech. 6 (2) (2004) 121–156.

[4] M. Bercovier, O. Pironneau, Error estimates for finite element method solution of the Stokes problem in primitive variables, Numer. Math. 33 (1979) 211–224.

[5] E. Dean, R. Glowinski, A wave equation approach to the numerical simulation of the Navier–Stokes equations for incompressible viscous flow, C.R. Acad. Sci. Paris 325 (Série I) (1997) 783–791.

[6] E. Dean, R. Glowinski, T.-W. Pan, A wave equation approach to the numerical simulation of incompressible viscous fluid flow modeled by the Navier–Stokes equations, in: J.A. De Santo (Ed.), Mathematical and Numerical Aspects of Wave Propagation, SIAM, Philadelphia, 1998, pp. 65–74.

[7] U. Ghia, K.N. Ghia, C.T. Shin, High-Reynolds solutions for incompressible flow using Navier–Stokes equations and a multigrid method, J. Comput. Phys. 48 (1982) 387–411.

[8] R. Glowinski, Finite element methods for incompressible viscous flow, in: P.G. Ciarlet, J.-L. Lions (Eds.), Handbook of Numerical Analysis, vol. IX, North-Holland, Amsterdam, 2003.

[9] R. Glowinski, L.H. Juárez, Finite element method and operator splitting for a time-dependent viscous incompressible free surface flow, Comput. Fluid Dyn. J. 12 (3) (2003) 459–468.

[10] J.G. Heywood, R. Rannacher, Finite element approximation of the non-stationary Navier–Stokes problem. I. Regularity of solutions and second-order error estimates for spatial discretization, SIAM J. Numer. Anal. 19 (2) (1982) 275–311.

[11] J.G. Heywood, R. Rannacher, Finite element approximation of the non-stationary Navier–Stokes problem, Part II: Stability of solutions and error estimates uniform in time, SIAM J. Numer. Anal. 23 (4) (1986) 750–777.

[12] G.I. Marchuk, Splitting and alternate direction methods, in: P.G. Ciarlet, J.-L. Lions (Eds.), Handbook of Numerical Analysis, vol. I, North-Holland, Amsterdam, 1990.

[13] C. Migeon, A. Texier, G. Pineau, Effects of lid-driven cavity shape on the flow establishment phase, J. Fluid Struct. 14 (2000) 469–488.

[14] T.W. Pan, R. Glowinski, A projection/wave-like equation method for the numerical simulation of incompressible viscous fluid flow modeled by the Navier–Stokes equations, Comput. Fluid Dyn. J. 9 (2) (2000) 28–42.

[15] O. Pironneau, Finite Element Methods for Fluids, Wiley, Chichester, 1989.

[16] R. Schreiber, H.B. Keller, Driven cavity flow by efficient numerical techniques, J. Comput. Phys. 40 (1983) 310–333.